Editors' Suggestion

On-demand magnon resonance isolation in cavity magnonics

Amin Pishehvar,[1] Zhaoyou Wang,[2] Yujie Zhu,[3] Yu Jiang,[1] Zixin Yan,[1] Fangxin Li,[2] Josep M. Jornet,[1] Jia-Mian Hu,[3] Liang Jiang,[2] and Xufeng Zhang[1,4,*]

[1] *Department of Electrical and Computer Engineering, Northeastern University, Boston, Massachusetts 02115, USA*

[2] *Pritzker School of Molecular Engineering, University of Chicago, Chicago, Illinois 60637, USA*

[3] *Department of Materials Science and Engineering, University of Wisconsin—Madison, Madison, Wisconsin 53706, USA*

[4] *Department of Physics, Northeastern University, Boston, Massachusetts 02115, USA*

(Received 18 September 2024; revised 28 November 2024; accepted 27 January 2025; published 20 February 2025)

Cavity magnonics is a promising field focusing on the interaction between spin waves (magnons) and other types of signal. In cavity magnonics, isolation of magnons from the cavity to allow signal storage and processing fully in the magnonic domain is highly desired, but its realization is often hindered by the lack of necessary tunability of the interaction. This work shows that by using the collective mode of two yttrium iron garnet spheres and applying Floquet engineering, magnonic signals can be switched on demand to a magnon dark mode that is protected from the environment, enabling a variety of manipulation over the magnon dynamics. Our demonstration can be scaled up to systems with an array of magnonic resonators, paving the way for large-scale programmable hybrid magnonic circuits.

DOI: 10.1103/PhysRevApplied.23.024053

I. INTRODUCTION

Dark mode [1] in electromagnetic devices is a phenomenon where a mode is isolated from the environment due to destructive interference or suppressed coupling. These modes often exhibit extended lifetimes because of reduced radiation emission into the environment, leading to important applications across a wide variety of platforms. For instance, in integrated photonics, dark modes are implemented in metasurfaces to achieve supercavity lasing [2–4]; in optomechanics, dark mode allows phonon-mediated quantum coupling between two optical resonators without the mechanical resonator being required to be cooled down to its quantum mechanical ground state [5–8]; while for superconducting qubits or cold atoms, dark mode is used to protect delicate quantum states [9,10].

In the emerging field of cavity magnonics [11–17], dark mode also finds important applications. Cavity magnonics studies the interaction between magnons and microwave photons in hybrid devices [18–24], with promising potential in coherent and quantum information processing [25–29]. Thanks to the large spin density in magnonic resonators, the coupling strength between magnons and photons can exceed their individual dissipation, bringing the system into the strong coupling regime, where information is exchanged between magnon and photon modes multiple times before decaying to below the noise level [18,30–32], enabling critical signal processing functionalities [33]. When multiple magnonic resonators couple with a single microwave cavity, collective magnon dark modes can form, which isolate magnons from the cavity [30,34], allowing the information to be stored in the magnonic domain and fully processed by magnonic approaches.

To harness the full potential of magnon dark modes, on-demand dark mode–bright mode conversion is required. However, such mode conversion is a fundamental challenge on all physical platforms, considering the isolated nature of the dark modes. It is worth noting that such on-demand conversion is fundamentally different—and thus should be differentiated—from the fixed dark mode–bright mode coupling, which is relatively easy to achieve [35–39]. Thus far, on-demand dark mode–bright mode conversion has been demonstrated only in very few systems, such as integrated photonics [40] and optomechanics [41]. In this work, we show that on-demand dark mode–bright mode conversion can be achieved on a magnetic platform. By application of Floquet engineering [42] to a multimode magnonic system, the magnon dark and bright modes can be coupled with a coupling strength determined by the amplitude and phase of a driving signal. This capability enables on-demand isolation of the giant spin ensemble from the microwave cavity, paving the way for advanced magnonic signal processing.

II. SYSTEM CONFIGURATION

Our device comprises a three-dimensional microwave cavity supporting a TE_{101} mode at $\omega_c = 2\pi \times 8.3$ GHz

*Contact author: xu.zhang@northeastern.edu

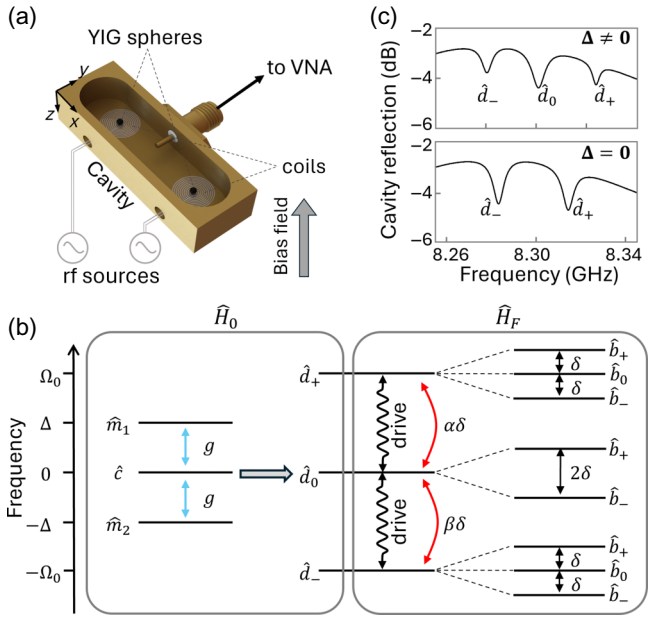

FIG. 1. (a) Device schematics. Two YIG spheres are placed at the center of two flat coils inside a copper cavity. The coils are parallel to the bias magnetic field to apply the Floquet drive. The coaxial probe is for microwave excitation and readout. (b) Energy level diagram. $\hat{m}_1$ ($\hat{m}_2$) is the first (second) magnon mode, $\hat{c}$ is the cavity mode, g is magnon-photon coupling strength, $\hat{d}_+$ ($\hat{d}_-$) is the upper (lower) hybrid mode, $\hat{d}_0$ is the center hybrid mode, $\alpha\delta$ is the energy level difference between $\hat{d}_0$ and $\hat{d}_+$, $\beta\delta$ is the energy level difference between $\hat{d}_0$ and $\hat{d}_-$, $\hat{b}_+$ ($\hat{b}_-$) is the upper (lower) Floquet hybrid mode, $\hat{b}_0$ is the center Floquet hybrid mode, and δ is energy level difference between two Floquet hybrid modes. (c) Reflection spectra of the microwave cavity. Top: Three modes ($\hat{d}_0$, $\hat{d}_+$, and $\hat{d}_-$) from the hybridization of one cavity mode and two magnon modes from the two YIG spheres. Bottom: The center mode ($\hat{d}_0$) becomes a dark mode and disappears when $\Delta = \omega_m - \omega_c = 0$. VNA, vector network analyzer.

with a quality factor of 2500 [Fig. 1(a)]. The cavity is probed by a coaxial probe via reflection measurement (S_{11}) with the use of a vector network analyzer. Two identical yttrium iron garnet (YIG) spheres (diameter of 0.4 mm) are positioned at the bottom of the cavity, each supporting a Kittel mode at frequency $\omega_n = \gamma H_n$, where H_n is the bias magnetic field for the nth ($n = 1, 2$) YIG sphere provided by a permanent magnet, and $\gamma = 2\pi \times 28$ GHz/T is the gyromagnetic ratio. To introduce Floquet drives to the magnon modes, a ten-turn flat coil is placed inside the cavity underneath each YIG sphere, with the coil axis parallel to the bias field direction (z direction).

This multimode Floquet cavity electromagnonic system can be described by the Hamiltonian $\hat{H}(t) = \hat{H}_0 + \hat{H}_F(t)$. The first term represents the conventional cavity electromagnonic system, which in the rotating frame of the cavity mode can be represented as

$$\hat{H}_0 = \hbar \sum_{n=1,2} \left[\Delta_n \hat{m}_n^\dagger \hat{m}_n + g_n(\hat{c}^\dagger \hat{m}_n + \hat{c}\hat{m}_n^\dagger)\right], \qquad (1)$$

where $\Delta_n = \omega_n - \omega_c$ is the frequency detuning of the nth magnon mode, g_n is the coupling strength between the nth magnon mode and the cavity mode, and $\hat{c}^\dagger$ and $\hat{c}$ ($\hat{m}_n^\dagger$ and $\hat{m}_n$) are the creation and annihilation operators, respectively, for the cavity mode (nth magnon mode) mode. Unless explicitly mentioned, we assume that $g_1 = g_2 = g$ and $\Delta_1 = -\Delta_2 = \Delta > 0$ throughout our analysis. The second term, $\hat{H}_F(t)$, represent the Floquet interaction:

$$\hat{H}_F(t) = \hbar \sum_{n=1,2} \epsilon_n \cos(\Omega_F t + \phi_n)\hat{m}_n^\dagger \hat{m}_n, \qquad (2)$$

where ϵ_n and ϕ_n are the amplitude and phase of the Floquet drive applied to the nth YIG sphere, respectively, and Ω_F is the frequency of the Floquet drive, which is assumed to be identical for both YIG spheres for simplicity.

The system can be illustrated by the energy level diagram in Fig. 1(b). The magnon modes (Kittel modes) of the two YIG spheres couple simultaneously to the same cavity mode, rending the two spheres an effective giant spin ensemble. In the absence of the Floquet drive, the two magnon modes form two ensemble modes $\hat{m}_B = (\hat{m}_1 + \hat{m}_2)/\sqrt{2}$ and $\hat{m}_D = (\hat{m}_1 - \hat{m}_2)/\sqrt{2}$. When both magnon modes are on resonance with the cavity ($\Delta = 0$), $\hat{m}_D$ does not couple with the cavity mode $\hat{c}$ (and thus is referred to as the "magnon dark mode" [30]), leading to the final dark mode $\hat{d}_0 = \hat{m}_D$, which cannot be observed in the cavity reflection spectrum, while $\hat{m}_B$ is coupled to the cavity mode $\hat{c}$ (accordingly referred to as the "magnon bright mode"), forming two new normal modes $\hat{d}_+$ and $\hat{d}_-$ at $\omega_c \pm \Omega_0$ [Fig. 1(c)]. Under this condition, the coupling of a single magnon mode with the cavity mode can be extracted from the splitting $g/2\pi = \Omega_0/2\sqrt{2}\pi = 12.6$ MHz. When the magnon modes are detuned ($\Delta \neq 0$), the magnon dark mode becomes "less dark" and gradually shows up in the cavity reflection spectrum.

III. DUAL-MODE FLOQUET MAGNONICS

When a Floquet drive with frequency $\Omega_F = \Omega_0$ is applied, it facilitates the interaction between the hybrid modes, as indicated by the Floquet Hamiltonian in the rotating frame of $\hat{H}_0$:

$$\hat{H}_F = \delta \hat{d}_0^\dagger(\alpha \hat{d}_+ + \beta \hat{d}_-) = \delta \hat{d}_0^\dagger \hat{d}_B, \qquad (3)$$

where α and β are the mixing coefficients [43]. Here $\hat{d}_B = \alpha \hat{d}_+ + \beta \hat{d}_-$ originates from the superposition of $\hat{d}_+$ and $\hat{d}_-$, which is referred to as the "Floquet bright mode" because it couples (assisted by the Floquet drive) to the

center mode $\hat{d}_0$ with a nonzero coupling strength δ, forming two new hybrid modes $\hat{b}_+$ and $\hat{b}_-$. In contrast, the orthogonal superposition mode $\hat{d}_D = \beta^* \hat{d}_+ - \alpha^* \hat{d}_-$ does not couple with the $\hat{d}_0$ mode, and thus is referred to as the "Floquet dark mode." The Floquet bright (dark) mode can also be viewed as the result of constructive (destructive) interference between the Floquet couplings from the $\hat{d}_+$ and $\hat{d}_-$ modes to the $\hat{d}_0$ mode. As a result of these interactions, the $\hat{d}_0$ mode splits into two levels associated with $\hat{b}_+$ and $\hat{b}_-$ that are separated by 2δ (assuming that $\alpha = \beta = 1$ for simplicity but without loss of generality), while the third level $\hat{b}_0 = \hat{d}_D$ disappears from the spectrum because of the canceled coupling. Similarly, $\hat{d}_+$ and $\hat{d}_-$ also split into two levels associated with $\hat{b}_+$ and $\hat{b}_-$ with a separation of 2δ. However, the coupling of $\hat{d}_0$ with $\hat{d}_+$ (or $\hat{d}_-$) does not cancel for the $\hat{d}_+$ mode (or the $\hat{d}_-$ mode), and therefore it can still be observed [$\hat{b}_0$ modes in Fig. 1(c)].

Figure 2 shows the measured cavity reflection spectra from a device with a nonzero magnon detuning ($\Delta > 0$). Three hybrid modes are observed, at 8.32103 GHz ($\hat{d}_+$), 8.30365 GHz ($\hat{d}_0$), and 8.28434 GHz ($\hat{d}_-$). When a Floquet drive is applied to both YIG spheres, Autler-Townes (AT) splittings show up on all three modes. As the drive frequency is tuned to match the level separation ($\Omega_F = \Omega_0 = 2\pi \times 18.55$ MHz), the Floquet bright mode $\hat{d}_B$ is fully hybridized with the center mode $\hat{d}_0$. Here the center mode $\hat{d}_0$ splits into two hybrid modes ($\hat{b}_+$ and $\hat{b}_-$), and no modes can be observed at the original frequency of the $\hat{d}_0$ mode, because the Floquet dark mode $\hat{d}_D$ completely decouples with the $\hat{d}_0$ mode. Once the drive frequency shifts away from Ω_0, the two hybrids are further apart, and a center mode gradually shows up because the Floquet dark mode is no longer completely "dark."

All the experimental observations in Fig. 2(a) agree very well with our numerical modeling (see Supplemental Material [43] for details), as shown by the calculated spectra in Fig. 2(b). The parameters used in the calculation are obtained through numerical fitting (for details, see Ref. [43]), which shows excellent agreement with the measurement results [Fig. 2(c)]. Our numerical fitting reveals that the Floquet drive on sphere 2 is 40% weaker than the Floquet drive on sphere 1, indicating that sphere 2 is mounted at a greater distance from the surface of the driving coil. This can also explain the dissipation rates ($\kappa_2/2\pi = 3.1$ MHz $< \kappa_1/2\pi = 6.3$ MHz) obtained via the same numerical fitting: sphere 1 suffers from higher losses due to closer proximity to the metallic coil. The spectra calculated with the same parameter set except for a 5 times reduction for all dissipation rates are shown in Fig. 2(d), revealing more spectral details for the multimode Floquet coupling. For example, the three modes split from $\hat{d}_+$ and $\hat{d}_-$ become clearly visible. In addition, it also shows that

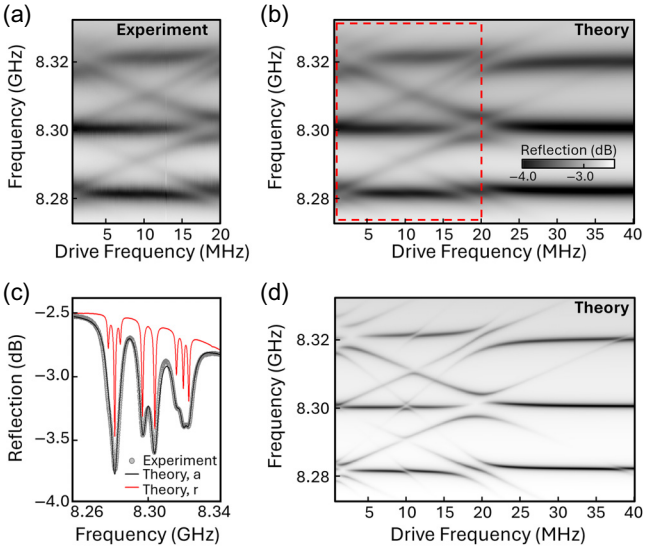

FIG. 2. (a) Measured and (b) calculated cavity reflection spectra as a function of driving frequency when both YIG spheres are driven. (c) Line plot of the measured cavity reflection (circles) and the numerical fitting (black line), together with calculation results with reduced linewidth (red). (d) Calculated cavity reflection spectrum obtained with reduced linewidth. "Theory, a" means theoretical value with actual linewidth; "Theory, r" means theoretical value with reduced linewidth.

the Floquet drive creates several high-order sidebands for each mode, which induce more anticrossing features when crossing the other modes. Direct coupling between the $\hat{d}_+$ and $\hat{d}_-$ modes without involving the $\hat{d}_0$ mode at a drive frequency $\Omega_F/2\pi$ of around 38 MHz is also observed but with much smaller splittings.

IV. PARAMETER DEPENDENCE

Under the dual-drive condition, the Floquet coupling strength obtained from our model is as follows [43]:

$$\delta = \frac{g\sqrt{(\epsilon_1^2 + \epsilon_2^2)(g^2 + \Delta^2) - 2\epsilon_1\epsilon_2 g^2 \cos(\phi)}}{2(2g^2 + \Delta^2)}, \quad (4)$$

where ϵ_n is the driving strength for the nth sphere and $\phi = \phi_1 - \phi_2$ is the phase difference between the two Floquet drives. The AT splitting between the $\hat{b}_+$ and $\hat{b}_-$ modes equals 2δ. According to Eq. (4), the AT splitting exhibits a linear dependence on the driving amplitude ϵ. This is confirmed by the extracted AT splittings at different driving amplitudes, as shown in Fig. 3(a). When a maximum driving amplitude (4 dBm) is applied, the AT splitting reaches 6.8 MHz. This value exceeds the dissipation rates of the interacting modes ($\kappa_0/2\pi = 2.6$ MHz, $\kappa_+/2\pi = 3.4$ MHz, $\kappa_-/2\pi = 2.55$ MHz), indicating that the Floquet drive–induced coupling has reached the strong coupling regime. The three-mode Floquet interaction also depends

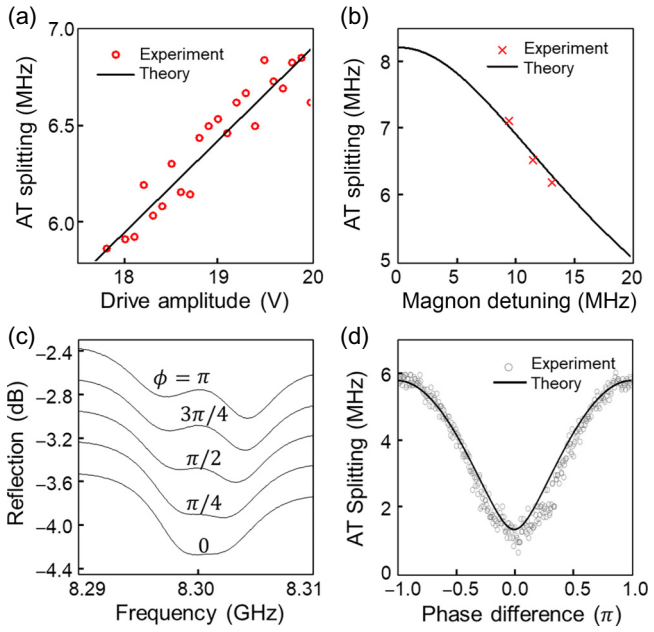

FIG. 3. AT splitting as a function of (a) the drive amplitude (here $\epsilon_1 = \epsilon_2$) and (b) magnon detuning. (c) Measured cavity reflection spectra at different phase differences ϕ between the two Floquet drives. (d) Extracted AT splitting as a function of the phase difference ϕ.

on the detuning Δ of the magnon modes. As the detuning reduces, the two hybrid modes $\hat{d}_+$ and $\hat{d}_-$ become closer in frequency, and accordingly smaller drive frequencies are required. In the meantime, a larger AT splitting is achieved [crosses in Fig. 3(b)], which agrees with the theoretical prediction obtained with Eq. (4) [solid line in Fig. 3(b)].

In our experiments, the measured AT splitting shows a strong dependence on the relative phase ϕ of the two Floquet drives for the two YIG spheres [Fig. 3(c)]. When the two drives are out of phase ($\pm\pi$), $\hat{d}_0$ exhibits maximum AT splitting, corresponding to the constructive interference of the coupling with the two modes $\hat{d}_+$ and $\hat{d}_-$, where the coupling of $\hat{d}_0$ with $\hat{d}_-$ and $\hat{d}_-$ is in phase and adds up to a stronger coupling. As ϕ decreases, the AT splitting becomes smaller, and reaches to a minimum when the two drives become in phase ($\phi = 0$). In this case, the couplings of $\hat{d}_0$ with $\hat{d}_+$ and $\hat{d}_-$ are out of phase and cancel each other, leading to diminished coupling. Such phase dependence can be conveniently explained by our model in Eq. (4). The calculated splitting is plotted as a function of ϕ [solid line in Fig. 3(d)], which shows good agreement with the experimental results. The nonzero minimum splitting at $\phi = 0$ can be attributed to the nonzero detuning of the magnon modes.

V. DARK MODE–BRIGHT MODE SWITCHING

On the basis the dual-mode Floquet coupling demonstrated above, controlled dark mode–bright mode switching can be achieved. In the spectra shown in Fig. 2(a), the detuning of the two magnon modes is not zero, and thus the center mode $\hat{d}_0$ is not a pure magnon dark mode $\hat{m}_D$ and thus can be observed. When the magnon detuning decreases, the center mode gradually disappears, as shown in Fig. 4(a). As Δ reaches zero, the center mode $\hat{d}_0$ becomes the magnon dark mode $\hat{m}_D$ and thus completely disappear from the spectrum [Fig. 4(a)(iv)]. However, its interaction with $\hat{d}_+$ and $\hat{d}_-$ still exists, as indicated by the AT splitting in the lower and upper levels. Although the AT splitting in the center mode cannot be directly measured, it can be revealed by our numerical modeling, as shown in Fig. 4(b)(ii), where a splitting is clearly visible in the center mode of the calculated spectra for the magnon dark mode $\hat{m}_D$. The validity of our model is verified by the calculated cavity reflection spectra [Fig. 4(b)(i)], which reproduced the experimental results in Fig. 4(a)(iv) with high accuracy.

Under the zero detuning condition $\Delta = 0$, the $\hat{d}_B$ mode equals the $\hat{m}_B$ mode, and accordingly Eq. (3) reduces to $\hat{H}_F = \delta \hat{m}_D^\dagger \hat{m}_B$. Therefore, the effect of the Floquet drive, which induces coupling between the center mode $\hat{d}_0$ and the two modes $\hat{d}_+$ and $\hat{d}_-$, is equivalent to inducing the coupling between the magnon dark and bright modes [Fig. 4(c)]. In this picture, the system consists of a cavity mode $\hat{c}$, a magnon bright mode $\hat{m}_B$, and a magnon dark mode $\hat{m}_D$. The interaction between the cavity and magnon bright modes is constantly on (with a coupling strength of $\sqrt{2}g$), while the interaction between the magnon dark and bright modes has a strength $\delta(\epsilon)$ that is controlled by the Floquet drive ϵ. Therefore, this enables the on-demand bright mode–dark mode switching, allowing the isolation of the magnon modes in the two YIG spheres from the cavity as needed with an electronic signal.

To demonstrate this capability, we performed a series of time-domain dynamical phase-field simulations based on coupled Maxwell-Landau-Lifshitz-Gilbert equations [44,45], which eliminated the practical limitation of the finite magnon lifetimes. The validity of the numerical simulation is confirmed by comparison with the calculated spectra. The simulation results for a dual-sphere system with $2\Omega_0/2\pi = 102$ MHz [which is different from the Ω_0 value used in Figs. 4(a) and 4(b)] and $\Delta = 0$ are plotted in Fig. 4(d); more simulation details can be found in Supplemental Material [43]. When a continuous-wave Floquet drive is applied (0–130 ns), the switching between the magnon dark and bright modes is constantly on, causing a Rabi-like oscillation between them after the dark mode is excited at $t = 0$. The rapid oscillation between $\hat{c}$ and $\hat{m}_B$ is due to the constantly on coupling between the two modes. When the system is in the magnon bright mode (130–160 ns), the application of a π pulse (at 160 ns) switches the system to the magnon dark mode. The system stays in the dark mode until another π pulse (at 200 ns)

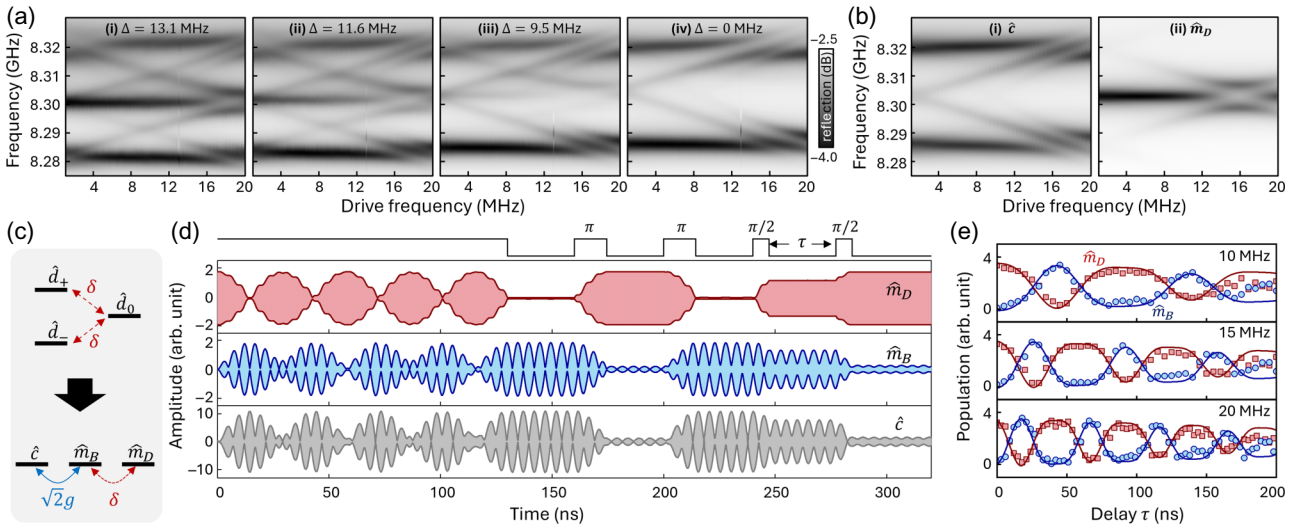

FIG. 4. (a) Measured cavity photon $\hat{c}$ reflection spectra at different magnon detunings: $\Delta = 13.2$, 11.6, 9.5, and 0 MHz. (b) Calculated spectra of the cavity photon $\hat{c}$ and magnon dark mode $\hat{m}_D$ obtained with the analytical model. (c) Effective energy diagram of the system. (d) Dynamical phase-field simulation results for the pulse response of the actual system in (a) with $\Delta = 0$ and $\Omega_F = \Omega_0$. The system is initially set to the $\hat{m}_D$ state at time zero. The top square waves show the Floquet drive pulses. (e) Magnon bright mode and dark mode amplitude obtained from the dynamical phase-field simulation at different drive detunings: $(\Omega_F - \Omega_0)/2\pi = 10$, 15, and 20 MHz. The signal is extracted after the application of a Ramsey pulse sequence and is plotted as a function of the delay between the two $\pi/2$ pulses. Red squares correspond to the dark mode from the simulation, blue circles correspond to the bright mode from the simulation, and solid lines are from the analytical calculation.

switches it back to the magnon bright mode. Although the constant $\hat{c}$–$\hat{m}_B$ coupling interferes with the magnon dark mode–bright mode switching, our numerical calculation shows that by one properly selecting the coupling strength and Floquet drive, it is possible to completely suppress this effect [43].

Moreover, the response of the system to Ramsey pulse sequences (i.e., two $\pi/2$ pulses with a varying delay τ) is also simulated. By adjustment of the detuning $(\Omega_F - \Omega_0)$ of the drive frequency in the Ramsey sequence, different interference fringes are observed [Fig. 4(e)]. As the detuning increases, the interference period becomes shorter, agreeing with the relation $T = 2\pi/(\Omega_F - \Omega_0)$. In conventional Ramsey interference experiments, which typically involve two interacting modes, the system experiences a relaxation period between the two $\pi/2$ pulses. However, in our three-mode system, there exists a constant interaction between the bright mode and the cavity mode. Consequently, the system stays for a shorter time in the $\hat{m}_B$ mode than in the $\hat{m}_D$ mode [43], exhibiting different interference fringes [Fig. 4(e)].

VI. CONCLUSION

We demonstrate a controlled approach that can isolate the magnon modes from the microwave cavity. Taking advantage of the collective mode in the effective giant spin ensemble formed by a dual-YIG-sphere system, the magnon dark mode can be switched on by means of an rf drive through the Floquet process, which was recently introduced to hybrid magnonics but was limited to hybrid modes only. Such a mechanism can be used to isolate and retrieve magnon signals from the cavity, which is one of the key functionalities that have been missing for coherent information processing in cavity magnonics. Our approach can be scaled up to more complex systems with multiple magnonic resonances, pointing to a new direction for achieving large-scale, programmable integrated magnonic circuits.

ACKNOWLEDGMENTS

X.Z. acknowledges support from the NSF (Grant No. 2337713) and the ONR Young Investigator Program (Grant No. N00014-23-1-2144). L.J. acknowledges support from the ARO (Grant No. W911NF-23-1-0077), the ARO Multidisciplinary University Research Initiative (Grant No. W911NF-21-1-0325), the AFOSR Multidisciplinary University Research Initiative (Grants No. FA9550-21-1-0209 and No. FA9550-23-1-0338), the NSF (Grants No. ERC-1941583, No. OMA-2137642, No. OSI-2326767, and No. CCF-2312755), and the Packard Foundation (Grant No. 2020-71479). The dynamical phase-field simulations in this work were supported by the U.S. Department of Energy, Office of Science, Basic Energy Sciences, under Award Number DE-SC0020145 as part of the Computational Materials Sciences Program (Y.Z. and J.-M.H.). The dynamical phase-field simulations were

performed with Bridges at the Pittsburgh Supercomputing Center through allocation TG-DMR180076 from the Advanced Cyberinfrastructure Coordination Ecosystem: Services & Support (ACCESS) program, which is supported by NSF Grants No. 2138259, No. 2138286, No. 2138307, No. 2137603, and No. 2138296. J.M.J acknowledges support from AFOSR (Grant No. FA9550-23-1-0254).

[1] H. Benisty, Dark modes, slow modes, and coupling in multimode systems, J. Opt. Soc. Am. B **26**, 718 (2009).
[2] M. V. Rybin, K. L. Koshelev, Z. F. Sadrieva, K. B. Samusev, A. A. Bogdanov, M. F. Limonov, and Y. S. Kivshar, High-Q supercavity modes in subwavelength dielectric resonators, Phys. Rev. Lett. **119**, 243901 (2017).
[3] M. Rybin and Y. Kivshar, Supercavity lasing, Nature **541**, 164 (2017).
[4] A. Kodigala, T. Lepetit, Q. Gu, B. Bahari, Y. Fainman, and B. Kanté, Lasing action from photonic bound states in continuum, Nature **541**, 196 (2017).
[5] C. Dong, V. Fiore, M. C. Kuzyk, and H. Wang, Optomechanical dark mode, Science **338**, 1609 (2012).
[6] Y.-D. Wang and A. A. Clerk, Using interference for high fidelity quantum state transfer in optomechanics, Phys. Rev. Lett. **108**, 153603 (2012).
[7] Y.-D. Wang and A. A. Clerk, Using dark modes for high-fidelity optomechanical quantum state transfer, New J. Phys. **14**, 105010 (2012).
[8] D.-G. Lai, X. Wang, W. Qin, B.-P. Hou, F. Nori, and J.-Q. Liao, Tunable optomechanically induced transparency by controlling the dark-mode effect, Phys. Rev. A **102**, 023707 (2020).
[9] M. Zanner, T. Orell, C. M. F. Schneider, R. Albert, S. Oleschko, M. L. Juan, M. Silveri, and G. Kirchmair, Coherent control of a multi-qubit dark state in waveguide quantum electrodynamics, Nat. Phys. **18**, 538 (2022).
[10] D. H. White, S. Kato, N. Német, S. Parkins, and T. Aoki, Cavity dark mode of distant coupled atom-cavity systems, Phys. Rev. Lett. **122**, 253603 (2019).
[11] B. Z. Rameshti, S. V. Kusminskiy, J. A. Haigh, K. Usami, D. Lachance-Quirion, Y. Nakamura, C.-M. Hu, H. X. Tang, G. E. Bauer, and Y. M. Blanter, Cavity magnonics, Phys. Rep. **979**, 1 (2022).
[12] M. Harder and C.-M. Hu, Cavity spintronics: An early review of recent progress in the study of magnon–photon level repulsion, Solid State Phys. **69**, 47 (2018).
[13] D. Lachance-Quirion, Y. Tabuchi, A. Gloppe, K. Usami, and Y. Nakamura, Hybrid quantum systems based on magnonics, Appl. Phys. Express **12**, 070101 (2019).
[14] B. Bhoi and S.-K. Kim, in *Solid State Physics* (Elsevier B.V., Amsterdam, 2020), Vol. 71, p. 39.
[15] Y. Li, W. Zhang, V. Tyberkevych, W.-K. Kwok, A. Hoffmann, and V. Novosad, Hybrid magnonics: Physics, circuits, and applications for coherent information processing, J. Appl. Phys. **128**, 130902 (2020).
[16] D. D. Awschalom, *et al.*, Quantum engineering with hybrid magnonic systems and materials (invited paper), IEEE Trans. Quantum Eng. **2**, 1 (2021).
[17] X. Zhang, A review of common materials for hybrid quantum magnonics, Mater. Today Electron. **5**, 100044 (2023).
[18] X. Zhang, C.-L. Zou, L. Jiang, and H. X. Tang, Strongly coupled magnons and cavity microwave photons, Phys. Rev. Lett. **113**, 156401 (2014).
[19] Y. Tabuchi, S. Ishino, T. Ishikawa, R. Yamazaki, K. Usami, and Y. Nakamura, Hybridizing ferromagnetic magnons and microwave photons in the quantum limit, Phys. Rev. Lett. **113**, 083603 (2014).
[20] M. Goryachev, W. G. Farr, D. L. Creedon, Y. Fan, M. Kostylev, and M. E. Tobar, High-cooperativity cavity QED with magnons at microwave frequencies, Phys. Rev. Appl. **2**, 054002 (2014).
[21] L. Bai, M. Harder, Y. P. Chen, X. Fan, J. Q. Xiao, and C.-M. Hu, Spin pumping in electrodynamically coupled magnon-photon systems, Phys. Rev. Lett. **114**, 227201 (2015).
[22] Y. Li, T. Polakovic, Y.-L. Wang, J. Xu, S. Lendinez, Z. Zhang, J. Ding, T. Khaire, H. Saglam, R. Divan, J. Pearson, W.-K. Kwok, Z. Xiao, V. Novosad, A. Hoffmann, and W. Zhang, Strong coupling between magnons and microwave photons in on-chip ferromagnet-superconductor thin-film devices, Phys. Rev. Lett. **123**, 107701 (2019).
[23] J. T. Hou and L. Liu, Strong coupling between microwave photons and nanomagnet magnons, Phys. Rev. Lett. **123**, 107702 (2019).
[24] Z.-Q. Wang, Y.-P. Wang, J. Yao, R.-C. Shen, W.-J. Wu, J. Qian, J. Li, S.-Y. Zhu, and J. Q. You, Giant spin ensembles in waveguide magnonics, Nat. Commun. **13**, 1 (2022).
[25] Y. Tabuchi, S. Ishino, A. Noguchi, T. Ishikawa, R. Yamazaki, K. Usami, and Y. Nakamura, Coherent coupling between a ferromagnetic magnon and a superconducting qubit, Science **349**, 405 (2015).
[26] D. Lachance-Quirion, S. P. Wolski, Y. Tabuchi, S. Kono, K. Usami, and Y. Nakamura, Entanglement-based single-shot detection of a single magnon with a superconducting qubit, Science **367**, 425 (2020).
[27] D. Lachance-Quirion, Y. Tabuchi, S. Ishino, A. Noguchi, T. Ishikawa, R. Yamazaki, and Y. Nakamura, Resolving quanta of collective spin excitations in a millimeter-sized ferromagnet, Sci. Adv. **3**, 00 (2017).
[28] S. P. Wolski, D. Lachance-Quirion, Y. Tabuchi, S. Kono, A. Noguchi, K. Usami, and Y. Nakamura, Dissipation-based quantum sensing of magnons with a superconducting qubit, Phys. Rev. Lett. **125**, 117701 (2020).
[29] D. Xu, X.-K. Gu, H.-K. Li, Y.-C. Weng, Y.-P. Wang, J. Li, H. Wang, S.-Y. Zhu, and J. Q. You, Quantum control of a single magnon in a macroscopic spin system, Phys. Rev. Lett. **130**, 193603 (2023).
[30] X. Zhang, C.-L. Zou, N. Zhu, F. Marquardt, L. Jiang, and H. X. Tang, Magnon dark modes and gradient memory, Nat. Commun. **6**, 1 (2015).
[31] T. Wolz, A. Stehli, A. Schneider, I. Boventer, R. Macêdo, A. V. Ustinov, M. Kläui, and M. Weides, Introducing coherent time control to cavity magnon-polariton modes, Commun. Phys. **3**, 1 (2020).
[32] M. Song, T. Polakovic, J. Lim, T. W. Cecil, J. Pearson, R. Divan, W.-K. Kwok, U. Welp, A. Hoffmann, K.-J. Kim, V. Novosad, and Y. Li, Programmable real-time magnon

interference in two remotely coupled magnonic resonators, ArXiv:2309.04289.

[33] J. Xu, C. Zhong, X. Han, D. Jin, L. Jiang, and X. Zhang, Coherent gate operations in hybrid magnonics, Phys. Rev. Lett. **126**, 207202 (2021).

[34] Y. Li, V. G. Yefremenko, M. Lisovenko, C. Trevillian, T. Polakovic, T. W. Cecil, P. S. Barry, J. Pearson, R. Divan, V. Tyberkevych, C. L. Chang, U. Welp, W.-K. Kwok, and V. Novosad, Coherent coupling of two remote magnonic resonators mediated by superconducting circuits, Phys. Rev. Lett. **128**, 047701 (2022).

[35] W. Cao, R. Singh, C. Zhang, J. Han, M. Tonouchi, and W. Zhang, Plasmon-induced transparency in metamaterials: Active near field coupling between bright superconducting and dark metallic mode resonators, Appl. Phys. Lett. **103**, 101106 (2013).

[36] X. Zhang, Q. Xu, Q. Li, Y. Xu, J. Gu, Z. Tian, C. Ouyang, Y. Liu, S. Zhang, X. Zhang, J. Han, and W. Zhang, Asymmetric excitation of surface plasmons by dark mode coupling, Sci. Adv. **2**, e1501142 (2016).

[37] S. R. K. Rodriguez, A. Abass, B. Maes, O. T. A. Janssen, G. Vecchi, and J. Gómez Rivas, Coupling bright and dark plasmonic lattice resonances, Phys. Rev. X **1**, 021019 (2011).

[38] S. Panaro, A. Nazir, C. Liberale, G. Das, H. Wang, F. De Angelis, R. Proietti Zaccaria, E. Di Fabrizio, and A. Toma, Dark to bright mode conversion on dipolar nanoantennas: A symmetry-breaking approach, ACS Photonics **1**, 310 (2014).

[39] F. Meng, F. Meng, L. Cao, L. Cao, A. Karalis, H. Gu, M. D. Thomson, H. G. Roskos, and H. G. Roskos, Strong coupling of plasmonic bright and dark modes with two eigenmodes of a photonic crystal cavity, Opt. Express **31**, 39624 (2023).

[40] M. Zhang, C. Wang, Y. Hu, A. Shams-Ansari, T. Ren, S. Fan, and M. Lončar, Electronically programmable photonic molecule, Nat. Photonics **13**, 36 (2019).

[41] D. P. Lake, M. Mitchell, B. C. Sanders, and P. E. Barclay, Two-colour interferometry and switching through optomechanical dark mode excitation, Nat. Commun. **11**, 1 (2020).

[42] J. Xu, C. Zhong, X. Han, D. Jin, L. Jiang, and X. Zhang, Floquet Cavity Electromagnonics, Phys. Rev. Lett. **125**, 237201 (2020).

[43] See Supplemental Material at http://link.aps.org/supplemental/10.1103/PhysRevApplied.23.024053 for details of device modeling, simulation, preparation, and measurements [46–51].

[44] J. Xu, C. Zhong, S. Zhuang, C. Qian, Y. Jiang, A. Pishehvar, X. Han, D. Jin, J. M. Jornet, B. Zhen, J. Hu, L. Jiang, and X. Zhang, Slow-wave hybrid magnonics, Phys. Rev. Lett. **132**, 116701 (2024).

[45] S. Zhuang, Y. Zhu, C. Zhong, L. Jiang, X. Zhang, and J.-M. Hu, Dynamical phase-field model of cavity electromagnonic systems, npj Comput. Mater. **10**, 1 (2024).

[46] X. Zhang, K. Ding, X. Zhou, J. Xu, and D. Jin, Experimental observation of an exceptional surface in synthetic dimensions with magnon polaritons, Phys. Rev. Lett. **123**, 237202 (2019).

[47] S. Zhuang, X. Zhang, Y. Zhu, N. X. Sun, C.-B. Eom, P. G. Evans, and J.-M. Hu, Hybrid magnon-phonon cavity for large-amplitude terahertz spin-wave excitation, Phys. Rev. Appl. **21**, 044009 (2024).

[48] S. Zhuang and J.-M. Hu, Acoustic attenuation in magnetic insulator films: Effects of magnon polaron formation, J. Phys. D: Appl. Phys. **56**, 054004 (2023).

[49] S. Zhuang and J.-M. Hu, Excitation and detection of coherent sub-terahertz magnons in ferromagnetic and antiferromagnetic heterostructures, npj Comput. Mater. **8**, 1 (2022).

[50] S. Zhuang, P. B. Meisenheimer, J. Heron, and J.-M. Hu, A narrowband spintronic terahertz emitter based on magnetoelastic heterostructures, ACS Appl. Mater. Interfaces **13**, 48997 (2021).

[51] A. Kamra, H. Keshtgar, P. Yan, and G. E. W. Bauer, Coherent elastic excitation of spin waves, Phys. Rev. B **91**, 104409 (2015).